AIAA JOURNAL
Vol. 44, No. 2, February 2006

High-Order Numerical Simulation of Turbulent Flow over a Wall-Mounted Hump

Philip E. Morgan,* Donald P. Rizzetta,† and Miguel R. Visbal‡
U.S. Air Force Research Laboratory, Wright–Patterson Air Force Base, Ohio 45433-7512

The development of a high-order spatial discretization for a k–ϵ turbulence model and its application to flow over a wall-mounted hump is described. The high-order implementation is validated for a flat plate and subsequently applied to the more complex wall-mounted hump for conditions with and without flow control. Results for the hump flow are compared to experimental data. The turbulence model is incorporated in an implicit parallel flow solver that is based on an approximately factored time-integration method coupled with spatially fourth- and sixth-order compact-difference formulations and a high-order filtering strategy. Both second-order and high-order discretizations of the k–ϵ turbulence equations were included in the compact solver. Validation using flow over a flat plate demonstrated that use of a second-order scheme for the k–ϵ turbulence equations dominates the solution even when high-order compact differencing is used for the flow equations. This validation also demonstrated that significant computational savings are possible because less mesh resolution is required when using a high-order discretization of the k–ϵ turbulence equations. Comparison of the high-order and second-order solutions was also performed for the wall-mounted hump. Qualitative agreement was achieved with experimental data for both high- and low-order schemes. High-order solutions on a coarse grid agreed very well with second-order solutions on a considerably finer grid.

Nomenclature

C_p	=	surface pressure coefficient, $2(p - p_\infty)/\rho_\infty U_\infty^2$
c	=	hump chord
E	=	total specific energy
$\boldsymbol{F}, \boldsymbol{G}, \boldsymbol{H}$	=	inviscid vector fluxes
$\boldsymbol{F}_v, \boldsymbol{G}_v, \boldsymbol{H}_v$	=	viscous vector fluxes
J	=	Jacobian of the coordinate transformation
M	=	Mach number
Pr	=	Prandtl number, 0.73 for air
Pr_t	=	turbulent Prandtl number, 0.90
p	=	nondimensional static pressure
$\boldsymbol{Q}$	=	vector of dependent variables
$\boldsymbol{q}_i$	=	components of the heat flux vector
Re_c	=	reference Reynolds number, $\rho_\infty u_\infty c/\mu_\infty$
T	=	nondimensional static temperature
t	=	nondimensional time
U, V, W	=	contravariant velocity components
u, v, w	=	nondimensional Cartesian velocity components in the x,y, and z directions
u_1, u_2, u_3	=	u, v, w
x, y, z	=	nondimensional Cartesian coordinates in the streamwise, vertical, and spanwise directions
x_1, x_2, x_3	=	x, y, z
γ	=	specific heat ratio, 1.4 for air
Δt	=	time step size
δ_{ij}	=	Kronecker delta function
μ	=	nondimensional molecular viscosity coefficient
μ_t	=	nondimensional eddy-viscosity coefficient
ξ, η, ζ	=	body-fitted computational coordinates
ρ	=	nondimensional fluid density
τ_{ij}	=	components of the viscous stress tensor

Presented as Paper 2004-2510 at the AIAA 2nd Flow Control Conference, Portland, OR, 28 June–1 July 2004; received 22 September 2004; revision received 13 April 2005; accepted for publication 21 April 2005.

*Senior Scientist, Ohio Aerospace Institute. Associate Fellow AIAA.
†Senior Research Aerospace Engineer, Computational Sciences Branch. Associate Fellow AIAA.
‡Technical Area Leader, Computational Sciences Branch. Associate Fellow AIAA.

I. Introduction

UNSTEADY separation control is a challenging area for numerical simulations.[1] This problem was again evident at the NASA Langley Research Center computational fluid dynamics (CFD) validation on synthetic jets and turbulent separation control workshop that was recently held. Specifically, the third case at this workshop, flow over a wall-mounted hump, proved difficult for participants to predict correctly the separated flow reattachment length downstream of the hump and the hump surface pressure coefficient. Because most participants applied second-order spatial discretization schemes, this work will focus on what improvement high-order numerical discretization of the turbulence equations could bring to this case. Hereafter the high-order spatial discretization of the flow and k–ϵ turbulence equations will be referred to as the high-order Reynolds-averaged Navier–Stokes equations (HO-RANS).

The experimental work for the NASA workshop[2,3] was based on a geometry and methodology similar to that used by Seifert and Pack.[1,4,5] Both uncontrolled and controlled flow conditions were investigated with multiple data acquisition methods including streamwise and spanwise pressure taps, extensive two-dimensional and three-dimensional particle image velocimetry (PIV), limited hot-wire and pitot tube measurements, and oil-film flow visualization for determining the reattachment location. The main objective of the NASA workshop was to develop a comprehensive database of an experiment with flow control for validation and comparison with CFD methods.

Except for one coarse direct numerical simulation,[6] all of the other numerical simulations applied either standard RANS or detached eddy simulations and hybrid RANS/large-eddy simulation (LES) methods. Unfortunately, independent of the approach employed, none of the participants achieved excellent agreement with the experimental data, especially when trying to match the hump surface pressure coefficient and the physics of the separated flow region downstream of the hump. These disagreements with experimental data were in part due to wind-tunnel blockage caused by the endplates that uniformly shifted the magnitude of the surface pressure coefficient; mostly they were due to the reliance on RANS models, which are generally unreliable for accurately simulating separated flow. Although these problems exist when trying to match

the experimental results, this case is still seen as valuable to explore with HO-RANS.

High-order schemes for solving the Navier–Stokes equations are prevalent for aeroacoustic, LES, direct numerical simulation (DNS), and other applications.[7] Although high-order schemes have seen multiple applications in these areas, few have included turbulence models. De Rango and Zingg[8] employed higher-order numerics for all components of their numerical scheme including two turbulence models, the algebraic Baldwin–Lomax and one-equation Spalart–Allmaras models. Their study on a NACA 0012 airfoil demonstrated that high-order algorithms significantly reduce computational costs and produce smaller errors on a given grid than second-order schemes on much finer meshes. Interestingly, the authors state, but do not quantify or demonstrate in this work and other works,[9–11] that the convective terms in the Spalart–Allmaras model could be reduced to first-order accuracy without introducing a significant source of error. Another recent application of a high-order spatial discretization of a turbulence models was a fifth-order accurate weighted essentially nonoscillatory scheme by Balakumar.[12] This work, also part of the NASA workshop, used the k–ω shear stress transport turbulence model for the wall-mounted hump simulation. Like the other methods at the workshop, this scheme had good qualitative agreement with experimental data but had problems accurately predicting the flow physics in the separated flow region downstream of the hump.

The high-order scheme, described in the Numerical Method section, has previously been used for multiple LES/DNS simulations including a supersonic cavity flowfield,[13] a supersonic compression ramp,[14] channel flow,[15] transitional flow over a circular cylinder,[15] and an airfoil.[16,17] Integrating HO-RANS will allow simulation of high Reynolds number flows and assist in development of high-order hybrid RANS/LES methods.

The main objective of the current work is to assess strengths and weaknesses of a HO-RANS approach for flowfields with flow control. The next two sections of this paper describe the governing equations and numerical scheme, respectively. The results section will cover validation of the compact discretization of the turbulence equations for flow over a flat plate and its application to the wall-mounted hump. The flow over the hump is simulated for conditions without flow control, steady suction, and oscillatory blowing and suction. Results are compared to available experimental data.

II. Governing Equations

The governing equations are the unsteady three-dimensional compressible mass-averaged Navier–Stokes equations. After transforming the equations from Cartesian coordinates to general time-dependent body-fitted curvilinear coordinates, the equations can be cast into strong conservation-law form as

$$\frac{\partial \boldsymbol{Q}}{\partial t}+\frac{\partial}{\partial \xi}\left(\boldsymbol{F}-\frac{1}{Re_\infty}\boldsymbol{F}_v\right)+\frac{\partial}{\partial \eta}\left(\boldsymbol{G}-\frac{1}{Re_\infty}\boldsymbol{G}_v\right)+\frac{\partial}{\partial \zeta}\left(\boldsymbol{H}-\frac{1}{Re_\infty}\boldsymbol{H}_v\right)=0 \tag{1}$$

Here t is the time, and ξ, η, and ζ are the computational coordinates. The vector of dependent variables is

$$\boldsymbol{Q}=(1/J)[\rho \quad \rho u \quad \rho v \quad \rho w \quad \rho E]^T \tag{2}$$

and the vector fluxes are given by

$$\boldsymbol{F}=\frac{1}{J}\begin{bmatrix}\rho U\\ \rho uU+\xi_x p\\ \rho vU+\xi_y p\\ \rho wU+\xi_z p\\ \rho EU+\xi_{x_i}u_i p\end{bmatrix}, \qquad \boldsymbol{G}=\frac{1}{J}\begin{bmatrix}\rho V\\ \rho uV+\eta_x p\\ \rho vV+\eta_y p\\ \rho wV+\eta_z p\\ \rho EV+\eta_{x_i}u_i p\end{bmatrix}$$

$$\boldsymbol{H}=\frac{1}{J}\begin{bmatrix}\rho W\\ \rho uW+\zeta_x p\\ \rho vW+\zeta_y p\\ \rho wW+\zeta_z p\\ \rho EW+\zeta_{x_i}u_i p\end{bmatrix} \tag{3}$$

$$\boldsymbol{F}_v=\frac{1}{J}\begin{bmatrix}0\\ \xi_{x_i}\tau_{i1}\\ \xi_{x_i}\tau_{i2}\\ \xi_{x_i}\tau_{i3}\\ \xi_{x_i}(u_j\tau_{ij}-q_i)\end{bmatrix}, \qquad \boldsymbol{G}_v=\frac{1}{J}\begin{bmatrix}0\\ \eta_{x_i}\tau_{i1}\\ \eta_{x_i}\tau_{i2}\\ \eta_{x_i}\tau_{i3}\\ \eta_{x_i}(u_j\tau_{ij}-q_i)\end{bmatrix}$$

$$\boldsymbol{H}_v=\frac{1}{J}\begin{bmatrix}0\\ \zeta_{x_i}\tau_{i1}\\ \zeta_{x_i}\tau_{i2}\\ \zeta_{x_i}\tau_{i3}\\ \zeta_{x_i}(u_j\tau_{ij}-q_i)\end{bmatrix} \tag{4}$$

where

$$U=\xi_t+\xi_{x_i}u_i, \qquad V=\eta_t+\eta_{x_i}u_i, \qquad W=\zeta_t+\zeta_{x_i}u_i \tag{5}$$

$$E=T\big/(\gamma-1)M_\infty^2+\tfrac{1}{2}(u^2+v^2+w^2) \tag{6}$$

In the preceding expressions, u, v, and w are the Cartesian velocity components, ρ the density, p the pressure, and T the temperature. All length scales have been nondimensionalized by the hump chord c, and dependent variables have been normalized by their reference values except for p, which has been nondimensionalized by $\rho_\infty u_\infty^2$. Components of the stress tensor and heat flux vector may be expressed as

$$\boldsymbol{q}_i=-\left[\frac{1}{(\gamma-1)M_\infty^2}\right]\left(\frac{\mu}{Pr}+\frac{\mu_t}{Pr_t}\right)\frac{\partial \xi_j}{\partial x_i}\frac{\partial T}{\partial \xi_j} \tag{7}$$

$$\tau_{ij}=(\mu+\mu_t)\left(\frac{\partial \xi_k}{\partial x_j}\frac{\partial u_i}{\partial \xi_k}+\frac{\partial \xi_k}{\partial x_i}\frac{\partial u_j}{\partial \xi_k}-\frac{2}{3}\delta_{ij}\frac{\partial \xi_l}{\partial x_k}\frac{\partial u_k}{\partial \xi_l}\right) \tag{8}$$

The Sutherland law for the molecular viscosity coefficient μ and the perfect gas relationship

$$p=\rho T\big/\gamma M_\infty^2 \tag{9}$$

were also employed. Stokes's hypothesis for the bulk viscosity coefficient has also been invoked.

The k–ϵ model has been chosen to calculate the eddy viscosity μ_t for RANS solutions. The standard Jones and Launder model with the low Reynolds number corrections of Launder and Sharma[18] is employed as described in Ref. 19. The k–ϵ equations, like the flow equations, can also be expressed in general curvilinear coordinates and conservation-law form as

$$\frac{\partial}{\partial \tau}\left(\frac{Q_t}{J}\right)+\frac{\partial \boldsymbol{F}_t}{\partial \xi}+\frac{\partial \boldsymbol{G}_t}{\partial \eta}+\frac{\partial \boldsymbol{H}_t}{\partial \zeta}+\boldsymbol{S}_t=\frac{1}{Re}\left[\frac{\partial \boldsymbol{F}_{vt}}{\partial \xi}+\frac{\partial \boldsymbol{G}_{vt}}{\partial \eta}+\frac{\partial \boldsymbol{H}_{vt}}{\partial \zeta}\right] \tag{10}$$

where the vectors of dependent variables and fluxes are

$$\boldsymbol{Q}_t=\begin{bmatrix}\rho k\\ \rho\epsilon\end{bmatrix}, \qquad \boldsymbol{F}_t=\frac{1}{J}\begin{bmatrix}\rho kU\\ \rho\epsilon U\end{bmatrix}, \qquad \boldsymbol{G}_t=\frac{1}{J}\begin{bmatrix}\rho kV\\ \rho\epsilon V\end{bmatrix}$$

$$\boldsymbol{H}_t=\frac{1}{J}\begin{bmatrix}\rho kW\\ \rho\epsilon W\end{bmatrix} \tag{11}$$

$$\boldsymbol{F}_{vt} = \frac{1}{J}\begin{bmatrix} \left(\mu + \frac{\mu_t}{\sigma_k}\right)\xi_{x_i}\frac{\partial \xi_j}{\partial x_i}\frac{\partial k}{\partial \xi_j} \\ \left(\mu + \frac{\mu_t}{\sigma_\epsilon}\right)\xi_{x_i}\frac{\partial \xi_j}{\partial x_i}\frac{\partial \epsilon}{\partial \xi_j} \end{bmatrix}$$

$$\boldsymbol{G}_{vt} = \frac{1}{J}\begin{bmatrix} \left(\mu + \frac{\mu_t}{\sigma_k}\right)\eta_{x_i}\frac{\partial \xi_j}{\partial x_i}\frac{\partial k}{\partial \xi_j} \\ \left(\mu + \frac{\mu_t}{\sigma_\epsilon}\right)\eta_{x_i}\frac{\partial \xi_j}{\partial x_i}\frac{\partial \epsilon}{\partial \xi_j} \end{bmatrix} \tag{12}$$

$$\boldsymbol{H}_{vt} = \frac{1}{J}\begin{bmatrix} \left(\mu + \frac{\mu_t}{\sigma_k}\right)\zeta_{x_i}\frac{\partial \xi_j}{\partial x_i}\frac{\partial k}{\partial \xi_j} \\ \left(\mu + \frac{\mu_t}{\sigma_\epsilon}\right)\zeta_{x_i}\frac{\partial \xi_j}{\partial x_i}\frac{\partial \epsilon}{\partial \xi_j} \end{bmatrix}$$

$$\boldsymbol{S}_t = \frac{1}{J}\begin{bmatrix} -(P_k - \rho\epsilon + D) \\ -\left(C_{\epsilon 1}P_k\epsilon/k - C_{\epsilon 2}f_{\epsilon 2}\rho\epsilon^2 + E_\epsilon\right) \end{bmatrix} \tag{13}$$

The turbulence Reynolds number and eddy viscosity coefficient are defined as

$$Re_t = Re(\rho k^2/\mu\epsilon), \qquad \mu_t = C_\mu f_\mu Re_t \mu \tag{14}$$

The production source term has been modified from the original formulation[19] to take the form

$$P_k = \left[\frac{\mu_t}{Re}\right]\left[\phi - \frac{2}{3}\left(\frac{\partial u_k}{\partial x_k}\right)^2\right] \tag{15}$$

where

$$\phi = |\omega| + 2\min(0, |s| - |\omega|) \tag{16}$$

where $|s|$ is the magnitude of the rate of strain tensor and $|\omega|$ is the magnitude of the vorticity. This formulation reduces the eddy viscosity in regions of the flow where vorticity exceeds the rate of strain, such as in a vortex core, and has minimal effect in shear layers.

To prevent anomalous behavior in regions where the the eddy viscosity should be near zero, the production term is limited as described in Ref. 19 to be

$$P_k = \min(P_k, 20.0\rho\epsilon) \tag{17}$$

For closure, the remaining parameters and functions are

$$f_\mu = \exp\left[\frac{-3.4}{(1 + 0.02Re_t)^2}\right], \qquad f_{\epsilon 2} = 1 - 0.3\exp\left(-Re_t^2\right) \tag{18}$$

$$D = -\frac{2\mu}{Re}\frac{\partial k^{\frac{1}{2}}}{\partial x_i}\frac{\partial k^{\frac{1}{2}}}{\partial x_i}, \qquad E_\epsilon = \left(\frac{2\mu\mu_t}{\rho Re^2}\right)\frac{\partial^2 u_i}{\partial x_j \partial x_j} + \frac{\partial^2 u_j}{\partial x_k \partial x_k} \tag{19}$$

with constants

$$\sigma_k = 1.0, \qquad \sigma_\epsilon = 1.3, \qquad C_\mu = 0.09$$
$$C_{\epsilon 1} = 1.44, \qquad C_{\epsilon 2} = 1.92 \tag{20}$$

Because this form of the k–ϵ model includes low Reynolds number terms to improve near-wall modeling, ϵ is formulated as the difference between the dissipation rate of the turbulent kinetic energy and the homogeneous turbulence. This formulation leads to both k and ϵ having homogeneous boundary conditions at solid walls.

III. Numerical Method

The solver advances the solution in time using a second-order implicit subiterative Beam–Warming algorithm.[20] The implicit, approximate-factorization, Beam–Warming algorithm[20] may be written in delta form as

$$\begin{aligned} &\left[I + \left(\frac{2\Delta t}{3}\right)\delta_{\xi 2}\left(\frac{\partial \boldsymbol{F}^p}{\partial \boldsymbol{Q}} - \frac{1}{Re_\infty}\frac{\partial \boldsymbol{F}_v^p}{\partial \boldsymbol{Q}}\right)\right] \\ &\quad\times\left[I + \left(\frac{2\Delta t}{3}\right)\delta_{\eta 2}\left(\frac{\partial \boldsymbol{G}^p}{\partial \boldsymbol{Q}} - \frac{1}{Re_\infty}\frac{\partial \boldsymbol{G}_v^p}{\partial \boldsymbol{Q}}\right)\right] \\ &\quad\times\left[I + \left(\frac{2\Delta t}{3}\right)\delta_{\zeta 2}\left(\frac{\partial \boldsymbol{H}^p}{\partial \boldsymbol{Q}} - \frac{1}{Re_\infty}\frac{\partial \boldsymbol{H}_v^p}{\partial \boldsymbol{Q}}\right)\right]\Delta \boldsymbol{Q} \\ &\quad= -\left(\frac{2\Delta t}{3}\right)\left[\left(\frac{1}{2\Delta t}\right)(3\boldsymbol{Q}^p - 4\boldsymbol{Q}^n + \boldsymbol{Q}^{n-1})\right. \\ &\quad+ \delta_\xi\left(\boldsymbol{F}^p - \frac{1}{Re_\infty}\boldsymbol{F}_v^p\right) + \delta_\eta\left(\boldsymbol{G}^p - \frac{1}{Re_\infty}\boldsymbol{G}_v^p\right) \\ &\quad\left.+ \delta_\zeta\left(\boldsymbol{H}^p - \frac{1}{Re_\infty}\boldsymbol{H}_v^p\right)\right] \end{aligned} \tag{21}$$

where $\partial \boldsymbol{F}/\partial \boldsymbol{Q}$, $\partial \boldsymbol{G}/\partial \boldsymbol{Q}$, and $\partial \boldsymbol{H}/\partial \boldsymbol{Q}$ are flux Jacobians, $\boldsymbol{Q}$ is the solution vector, and δ represents the spatial difference operator. Newton-like subiterations (see Ref. 21) are incorporated into the scheme to recover temporal accuracy and stability properties of the algorithm due to errors introduced by linearization, factorization, and explicit updating of boundary conditions and overset grid interfaces. Subiterations also permit the use of the more efficient diagonal form[22] of the implicit algorithm while retaining time accuracy. The subiterate is given by $\Delta \boldsymbol{Q} = \boldsymbol{Q}^{p+1} - \boldsymbol{Q}^p$, where p denotes the number of subiterations. For the first solver application ($p = 1$), $\boldsymbol{Q}^p = \boldsymbol{Q}^n$, where n is the solution time level. With subsequent subiterations, $\boldsymbol{Q}^{p+1} \to \boldsymbol{Q}^{n+1}$. Based on previous unsteady flow computations, three applications of the solver per time step are typically found to be sufficient to recover second-order time accuracy.[23–25]

The k–ϵ equations and Navier–Stokes equations are uncoupled in the implicit solution procedure. The eddy viscosity is lagged from the previous iteration when the flow variables are solved, and the mean flow variables are lagged when the turbulence model is solved. To recover time accuracy, enhance stability, and relieve stiffness of the k–ϵ equations, the turbulence model is solved every time step and subiteration.

The implicit portion of the algorithm uses second-order accurate three-point backward differencing for the time derivative and second-order central finite difference approximations for the spatial derivatives [denoted with the subscript 2 in Eq. (21)]. Nonlinear artificial dissipation terms (not shown) are appended to the implicit operator to enhance stability. The spatial derivatives on the right-hand side of Eq. (21) use high-order compact-difference operators that recover higher-order spatial accuracy with subiterations.

The high-order spatial derivatives on the right-hand side of the governing equation are discretized using the compact finite difference scheme of Lele,[26] which can attain spectrallike resolution. With use of the tridiagonal subset of this scheme, the spatial derivative of any scalar f, such as a metric, flux component, or flow variable, can be obtained by solving the system

$$\begin{aligned} &\alpha\left(\frac{\partial f}{\partial \xi}\right)_{i-1} + \left(\frac{\partial f}{\partial \xi}\right)_i + \alpha\left(\frac{\partial f}{\partial \xi}\right)_{i+1} \\ &\quad= a\left(\frac{f_{i+1} - f_{i-1}}{2}\right) + b\left(\frac{f_{i+2} - f_{i-2}}{4}\right) \end{aligned} \tag{22}$$

where α, a, and b determine the spatial properties of the algorithm. The present investigation employed the compact sixth-order (C6) and fourth-order (C4) schemes, corresponding to $\alpha = 1/3, a = 14/9$, and $b = 1/9$ and $\alpha = 1/4$, $a = 3/2$, and $b = 0$, respectively.

Dispersion-error characteristics and truncation error of these schemes are discussed in detail in Refs. 26 and 27. Also discussed in Ref. 27 are descriptions of the higher-order one-sided formulas used near boundaries.

To control numerical instabilities, a general high-order (up to 10th-order) low-pass Padé-type spatial filter has been incorporated into the compact difference scheme.[28] These nondispersive spatial filters have been demonstrated as superior to explicit artificial viscosity even on generalized curvilinear meshes. The filter is applied to the solution vector $\boldsymbol{Q}$ in each of the three computational directions following each subiteration. The filtered values of the solution vector are obtained by solving the tridiagonal system

$$\alpha_f \check{\boldsymbol{Q}}_{i-1} + \check{\boldsymbol{Q}}_i + \alpha_f \check{\boldsymbol{Q}}_{i+1} = \sum_{n=0}^{N} \frac{a_n}{2} (\boldsymbol{Q}_{i+n} + \boldsymbol{Q}_{i-n}) \tag{23}$$

where $\check{\boldsymbol{Q}}$ is the filtered value of $\boldsymbol{Q}$ and α_f is a free parameter for this family of filters, which must remain in the range $-0.5 \le \alpha_f \le 0.5$. Higher values of α_f correspond to less dissipative filters. The coefficients a_n in Eq. (23) are summarized in Ref. 27. The choice of N provides a $2N$th-order filter. On uniform meshes, these filters preserve constant functions, completely eliminate the odd–even mode decoupling, and do not amplify waves.[29] Low-pass filtering provides dissipation at the high modified wave numbers only where the spatial discretization already exhibits significant dispersion errors, whereas nonspectral-based artificial viscosity and upwind-biased schemes introduce dissipation across a wide range of wave numbers.

Filtering near any domain boundary requires the implementation of one-sided, high-order, Padé-type formulas as discussed in Refs. 27 and 28. Unlike the interior filter, the one-sided high-order filters can amplify wave amplitudes for certain range of wave numbers. To eliminate this undesirable amplification behavior, higher values of α_f are sometimes required near boundaries.[30]

The described components are implemented in a parallel scheme based on an overset grid methodology. The current cases use direct injection between overlapping blocks. The overset grid methodology is used in conjunction with the message-passing interface (MPI) library for interblock communication. The resulting MPI code has been successfully ported to several parallel platforms. Additional background on the parallel compact solver is covered in detail in Ref. 15.

IV. Results

A. Flat Plate

Turbulent flow over a flat plate is used for validation of the HO-RANS methodology and to develop the inflow conditions for flow over the wall-mounted hump. Because the flat plate solution provides the inflow profile for the wall-mounted hump, the reference flow conditions of $M_\infty = 0.10$ and $Re_c = 9.36 \times 10^5$ are used for both cases.

The computational domain for the flat plate extended from $-2.0 \le x \le 6.5$ in the streamwise direction and from $0.0 \le y \le 0.9090$ in the normal direction. The streamwise portion of the mesh had 801 points, which were uniformly distributed with a $\Delta x = 0.001$ from the inflow to $x = 5.8$ and stretched from there to the end of the domain. The grid distribution in the normal direction was extracted from the wall-mounted hump grid provided by the NASA workshop. The fine grid distribution had 217 points with clustering near the flat plate surface. The first point off the wall was located at $y = 8.0 \times 10^{-6}$, which corresponds to a $\Delta y^+ = 0.28$ at the streamwise location, which matches the momentum thickness of the experimental inflow profile. A coarse mesh was derived from the fine mesh by eliminating every other point in the normal direction. This approach led to a coarse mesh wall spacing of $\Delta y^+ = 0.60$.

The flat plate simulation was performed twice with different boundary conditions. The first time, the simulation was accomplished using a finite flat plate that started at $x = 0.0$. In this case the inflow, at $x = -2.0$, was prescribed as uniform flow with velocities of $u = 1$ and $v = w = 0$ and density of $\rho = 1$. The inflow pressure was updated by imposing a zero streamwise pressure gradient. A symmetry boundary condition was prescribed along the bottom of the domain from the inflow to the leading edge of the flat plate. The flat plate, also at the bottom of the domain, enforced isothermal, no-slip flow conditions and a zero normal pressure gradient. An inviscid wall was imposed at the top of the domain. The outflow velocities and density were extrapolated using a streamwise Neumann boundary condition, and pressure was set to its freestream value. The values of k and ϵ were prescribed to zero at the surface of the flat plate, freestream values at the inflow, and extrapolated for all other boundaries. The second simulation changed two boundary conditions. The bottom domain was changed from a flat plate with a leading edge to a flat plate that extended over the entire streamwise domain. The other change was that the inflow was now prescribed using a fully developed turbulent profile computed in the first simulation.

The finite flat plate case was initialized with uniform flow ahead of the flat plate and with Prandtl's one-seventh power-law profile for the turbulent boundary layer over the flat plate. The second simulation, where the flat plate spans the entire streamwise domain, used a fully developed turbulent profile from the previous simulation. A time step of $0.0001 \le \Delta t \le 0.00025$ was used for all computations. All simulations were advanced to the nondimensional time $t = 20$.

Three mixes of flow/turbulence model spatial discretization order were investigated for the flat plate flow. The three combinations are second-order Navier–Stokes equations and turbulence equations case, sixth-order flow and second-order turbulence equations, and sixth-order flow and turbulence equations. Hereafter these are referred to as C2KE2, C6KE2, and C6KE6, respectively. Note that to control numerical instabilities, the HO-RANS approach uses filtering instead of explicit artificial viscosity, which is commonly used with second-order accurate RANS turbulence models.

Coarse and fine grid results for these three cases are shown in Figs. 1 and 2, respectively. Displayed are the velocity profiles in

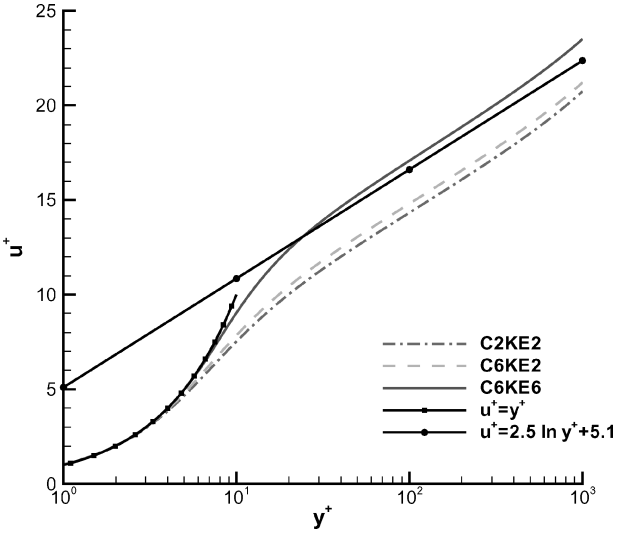

Fig. 1 Turbulent flat plate velocity profile for coarse grid.

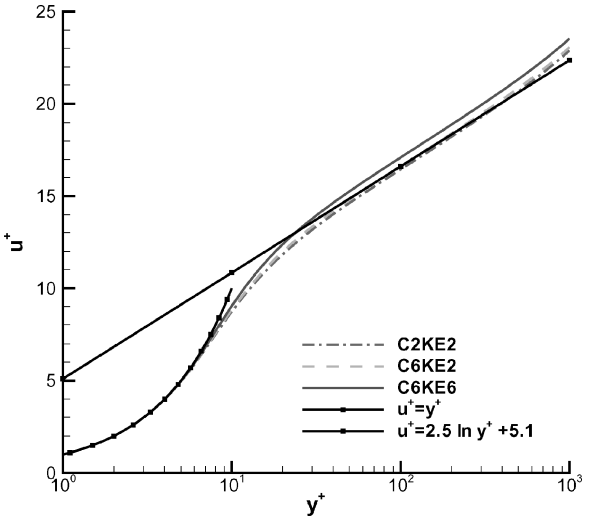

Fig. 2 Turbulent flat plate velocity profile for fine grid.

terms of sublayer scaled length and velocity variables y^+ and u^+ for the computations and the empirical viscous sublayer and the log law relations. One finding that can be drawn from these results is that increasing the spatial discretization order of the flow equations while keeping a second-order k–ϵ turbulence model, that is, cases C2KE2 and C6KE2, has minimal influence on the resulting velocity profile as seen on both the coarse and fine grid. Thus, it can be concluded that to have a high-order solution the discretization order of the flow and the k–ϵ turbulence equations must both be high order. Another result of this test demonstrates the well-known fact that high-order schemes achieve grid-independent solutions quicker than second-order schemes. This can be seen by comparing the solutions on the coarse and fine grid. The sixth-order solution agreed exceptionally well with the empirical data on both grids and was virtually unchanged as the mesh was refined. The second-order solution shows significant improvement in agreement with the empirical solutions as the grid was refined. This result demonstrates that the high-order solver can achieve a grid-converged result on a mesh that is less than half that required by a standard second-order scheme. Because using the compact solver increased the computational work by only about 50%, there was a significant reduction in the net computational cost. The next problem reinforces this finding because the compact solver needed a mesh only one-fourth the size required by the second-order scheme to arrive at an equivalent solution.

B. Wall-Mounted Hump

With the validation of the HO-RANS technique complete for a simple flat plate, the investigation was continued for the more complex wall-mounted hump. The hump geometry simulates the upper surface of a 20% thick Glauert–Goldschmied airfoil. The wall-mounted hump has a chord length of 0.4200 m, a maximum height of 0.0537 m, and a span of 0.5842 m. A slot was located at approximately 65% chord for flow control. The body definition is shown in Fig. 3. The flow conditions for the experiment were, as with the flat plate, $M_\infty = 0.10$ and $Re_c = 9.36 \times 10^5$. The baseline case consists of no suction or blowing through the slot, although the slot was left open to interact with the flow over the hump. Two flow control cases were also simulated, one using constant suction through the slot at a rate of 0.01518 kg/s and the other using a zero-efflux oscillatory jet produced by a rigid piston at the bottom of the plenum, which generated a maximum outward slot velocity of 26.6 m/s. Significant effort was expended by the experimental setup to access the two dimensionality of the flow. The experimentalist concluded[2,3] that use of two-dimensional unsteady RANS (URANS) simulations would be justifiable for the flow over the wall-mounted hump for both the baseline and flow control cases. Three-dimensional URANS simulations were performed for the current geometry and verified that the flow was essentially two dimensional.

The computational and experimental domains for the hump and wind tunnel extend from $x = -2.14$ to $x = 4.0$ in the streamwise direction and from $y = 0.0$ to $y = 0.9090$ in the normal direction.

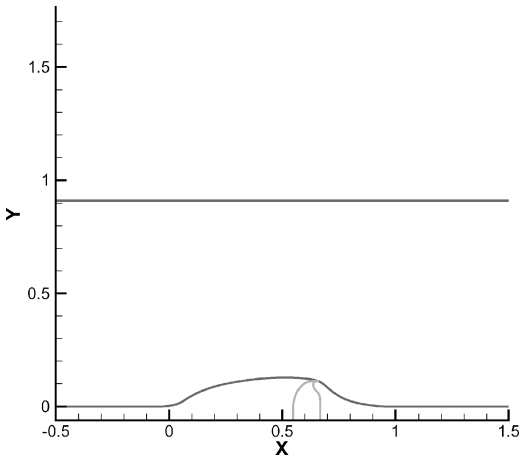

Fig. 3 Wall-mounted hump.

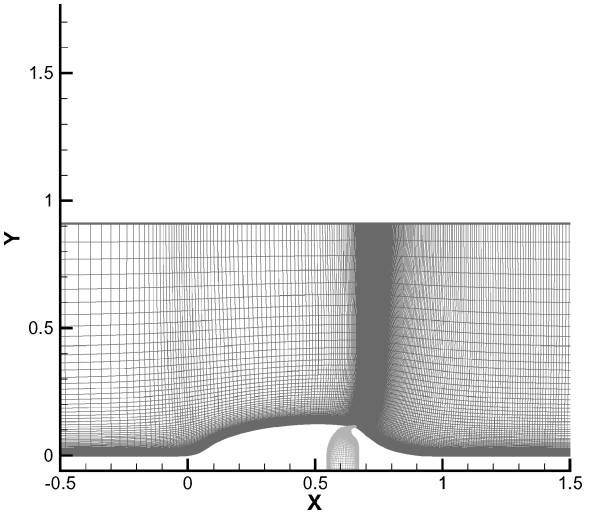

Fig. 4 Coarse grid for hump and slot.

The physical domain was nondimensionalized by the length of the hump and was located between $0.0 \le x \le 1.0$.

Two grids have been used during the course of this study. The first mesh employed a elliptically smoothed version of the grid provided by the organizers of the NASA workshop. The second grid was generated using the scaled two-dimensional hump coordinate database, which was also provided, and the normal grid distribution from the first mesh. Both meshes consisted of two blocks and had the same dimensions. The first grid block contained the hump and interior of the wind tunnel using 793×217 points in the streamwise and normal directions, respectively. The normal grid distribution was identical for both grids and is described for the preceding flat plate case. The second mesh block defines the slot used for flow control. It has 225 grid points in the direction that connects the bottom of the plenum to the slot opening and either 121 points (NASA grid) or 81 points (database-generated mesh) spanning the width of the slot. The only modification made to the NASA provided mesh was that the two-block grid was smoothed while enforcing orthogonality at the walls using the elliptic solver in GRIDGEN.[31] Finally, for both grids the slot mesh had to be extended five points into the hump grid to produce an overset topology. The final database-generated mesh is shown in Fig. 4. Coarse grids were extracted from these two fine grids by eliminating every other point in each coordinate direction.

Boundary conditions used in the simulations include: isothermal, no-slip walls for the lower plate surface, the hump, and walls of the slot; inviscid wall boundary conditions for the top of the wind tunnel; prescribed velocities and density with pressure updated via Neumann boundary condition at the tunnel inflow; and pressure fixed to freestream value and all other variables updated using Neumann boundary conditions at the outflow. Inflow profiles for the coarse and fine grids were extracted from the corresponding C6KE6 flat plate RANS calculations described earlier. The flat plate profiles used for the hump inflow match the momentum thickness of the experimental inflow profile. Figure 5 shows the comparison of the coarse and fine grid inflow profiles with experimental data. The bottom of the cavity treated all quantities as an inviscid wall. At this wall, the v component of velocity had three possible boundary conditions. For the baseline no-flow control case, v is set to zero at the bottom of the cavity. For the suction case, the velocity was prescribed to $v = -0.012475$ to match the given mass flow rate of 0.01518 kg/s through the 0.5842-m-wide slot. For the oscillatory blowing and suction case, the velocity was defined by $v = A \sin(\omega t)$, where $A = 9.39 \times 10^{-3}$, $\omega = 2\pi f$, and $f = 138.5$ Hz to match the maximum slot velocity of 26.6 m/s. The two-dimensional coarse mesh cases were initialized using the inflow profile for the wind tunnel/hump mesh and stagnation flow for the slot and cavity. The cavity pressure, density, and turbulence variables (k and ϵ) were set to the value one point away from the wall given in the inflow profile. Results shown for the hump are time averaged over the

Table 1 Case summary

Case	Grid	Scheme order	$\Delta\tau$
C2KE2C	Coarse	Second	1.0×10^{-4}
C2KE2F	Fine	Second	5.0×10^{-5}
C4KE4C	Coarse	Fourth	1.0×10^{-4}

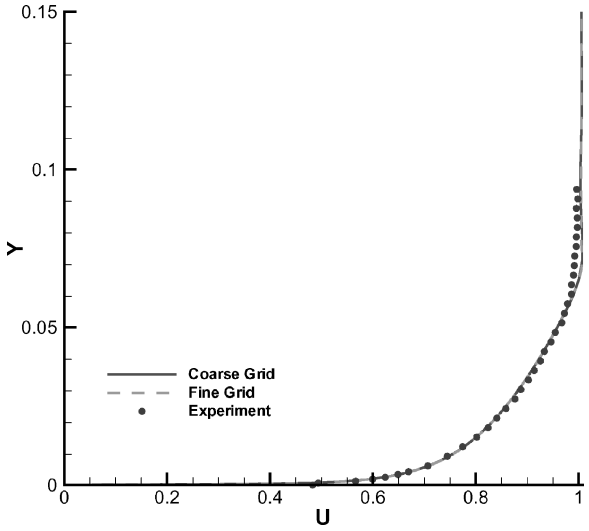

Fig. 5 *U*-velocity profile comparison at inflow.

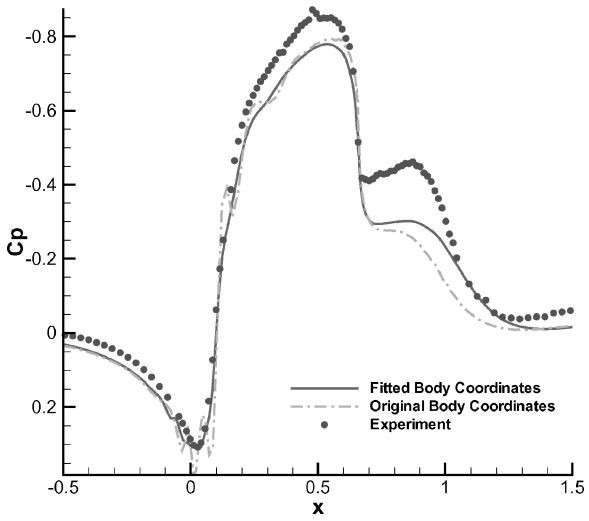

Fig. 6 Pressure coefficient comparison of original and fitted-body grids.

interval $0 \leq t \leq 25$. To ensure convergence, the time-averaged pressure coefficient, skin-friction coefficient, and velocity profiles were compared every 100,000 time steps. No changes were evident in the monitored quantities, thus, suggesting that a steady state had been achieved.

A summary of the multiple simulations completed for the wall-mounted hump geometry are given in Table 1. Discussion of results will focus on effects of grid resolution and spatial scheme accuracy.

The baseline case with no flow control will be discussed before looking at cases with flow control. Preliminary calculations on the coarse grid provided by the workshop organizers showed significant local oscillations in the surface pressure coefficient C_p when using fourth-order discretizations as seen in Fig. 6. The source of the oscillations was determined to be due to small discontinuities in the surface body definition. These can be easily seen by looking at the second derivative of the surface geometry, that is, the surface curvature, shown in Fig. 7. Second-order schemes have

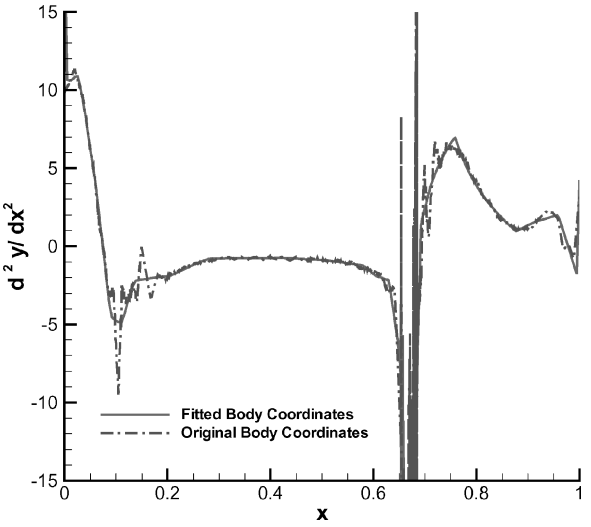

Fig. 7 Curvature comparison of original and fitted-body coordinates.

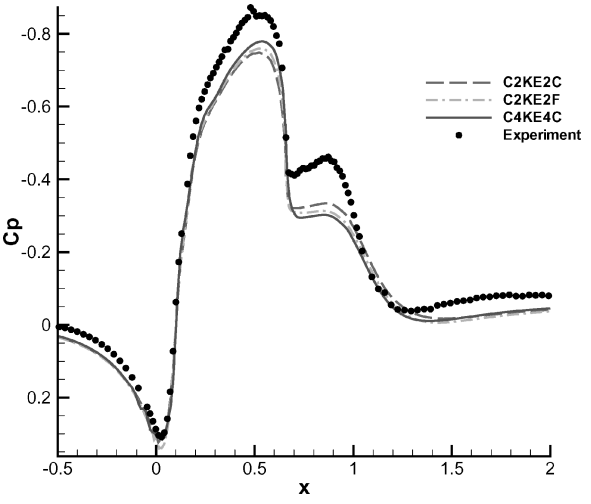

Fig. 8 Baseline case: surface pressure coefficient comparison.

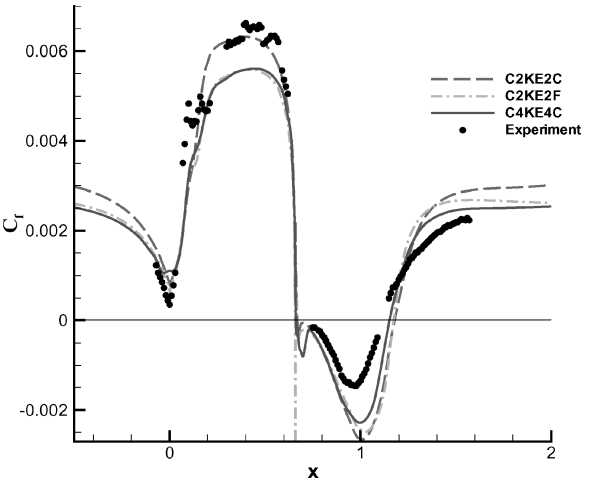

Fig. 9 Baseline case: skin-friction coefficient comparison.

enough dissipation to negate these small discontinuities, but the fourth-order scheme is greatly influenced by them. The discontinuities can be smoothed out by generating a fitted-cubic polynomial curve from the original body database using algorithms available with the GRIDGEN software. The fitted geometry differed from the original nondimensionalized geometry by less than $y \leq 1.0 \times 10^{-4}$. Results of smoothing the body database can be seen in Fig. 6, which now has an almost oscillation free C_p. No other stability problems

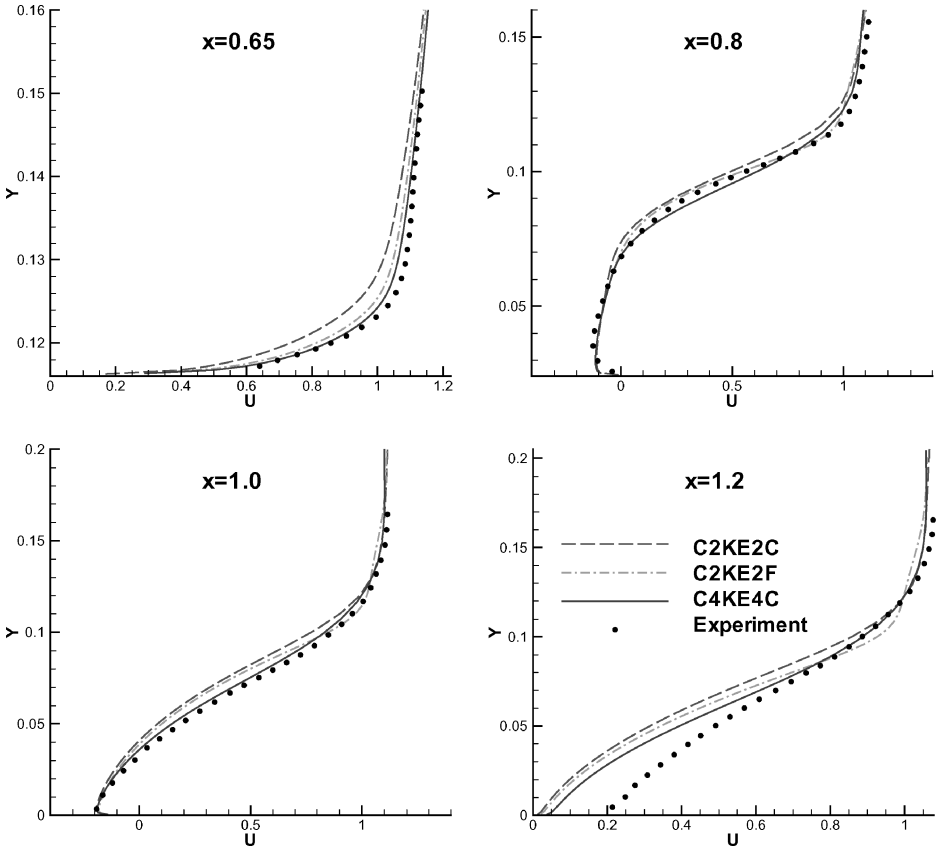

Fig. 10 Baseline case: *U*-velocity profile comparison at $x = 0.65$, 0.8, 1.0, and 1.2.

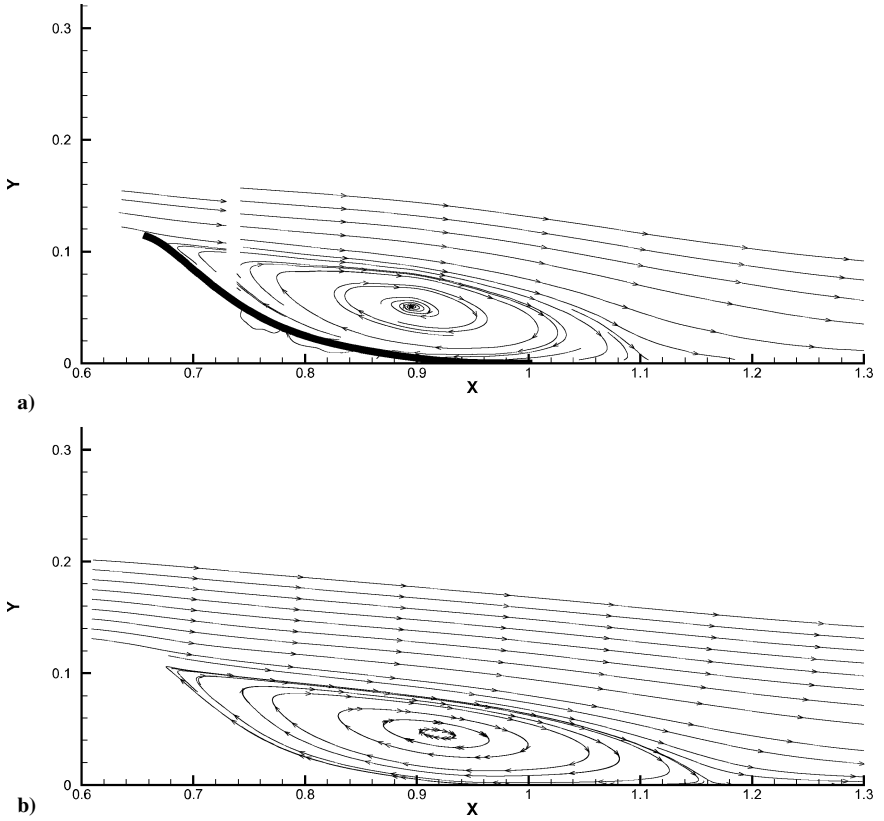

Fig. 11 Baseline case: comparison of a) experimental PIV and b) numerical streamlines.

were present in the scheme due to grid clustering near boundaries and the slot. A very through evaluation and discussion on effects of mesh-spacing discontinuities, localized abrupt grid skewing, and mesh distortion for the compact high-order scheme can be found in Visbal and Gaitonde.[32]

The surface pressure coefficient for the different schemes and grids is shown in Fig. 8. The computed results have a smaller C_p magnitude than the experiment over the mid-portion of the hump and in the recirculation region downstream of the hump. This trend was also seen by most of the participants of the NASA workshop and was later found to be partially due to wind tunnel blockage caused by the endplates in the experimental setup. Using high-order discretization, case C4KE4C, and finer grid resolution, case C2KE2F, does improve agreement with the experiment in the midspan of the hump, but also results in more discrepancy in the recirculation region.

A comparison of the skin-friction coefficient C_f is shown for the different methods in Fig. 9. Also shown in Fig. 9 is a line at $C_f = 0$ to delineate between attached and separated flow. All of the cases qualitatively agree, but significantly better agreement exists between the high-order solution and the fine grid second-order result. In the recirculation region, slightly better agreement with experimental data is achieved by using the high-order scheme. A summary of reattachment points is given in Table 2.

The u-velocity profiles just before the slot at $x = 0.65$, at two locations in the recirculation region ($x = 0.8$ and $x = 1.0$) and finally right after flow reattachment at $x = 1.2$ are shown in Fig. 10. Near the slot, both just upstream and downstream of the slot, the u component of velocity shows very good agreement when the flow is resolved, as in cases C2KE2F and C4KE4. At $x = 1.0$, the high-order

Table 2 Hump flow reattachment location summary

	Reattachment location, x		
Case	Baseline	Suction	Oscillatory
C2KE2C	1.18	1.08	1.27
C2KE2F	1.17	1.13	1.23
C4KE4C	1.15	1.08	1.33
Experiment	1.11 ± 0.003	0.94 ± 0.005	0.98

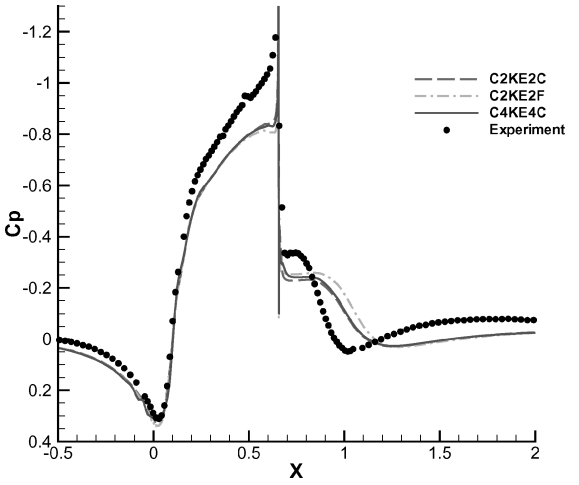

Fig. 13 Suction case: surface pressure coefficient comparison.

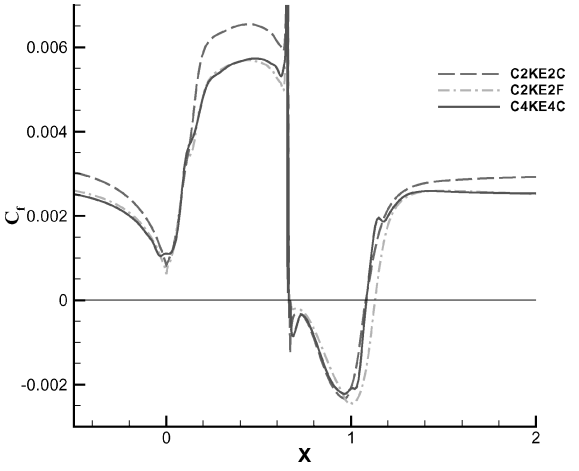

Fig. 14 Suction case: skin-friction coefficient comparison.

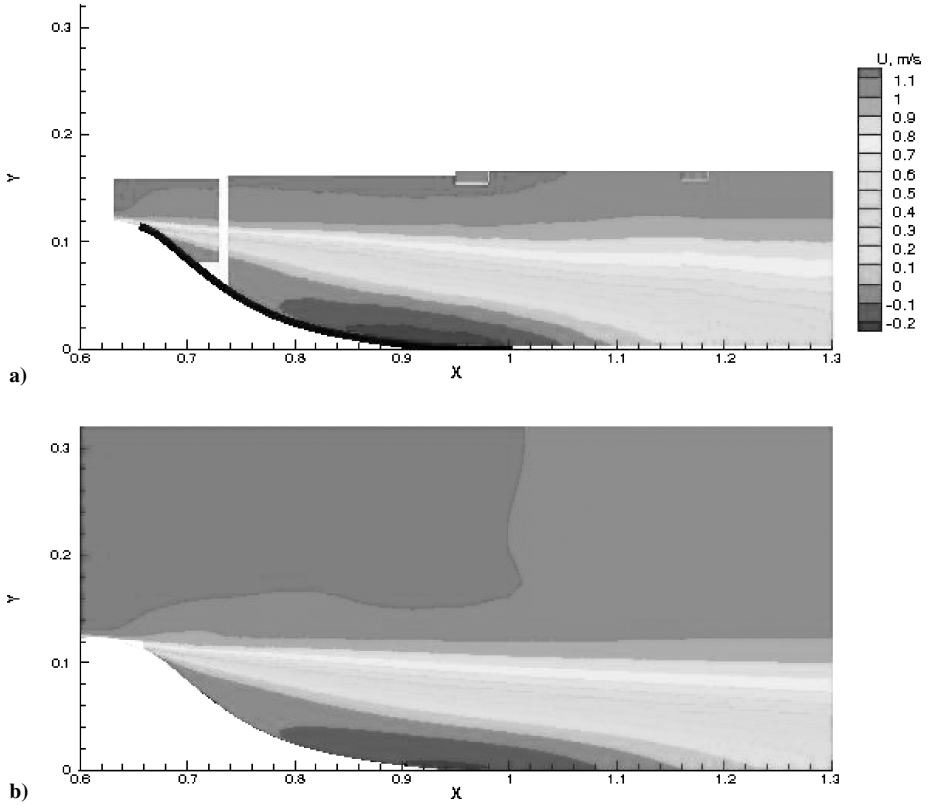

Fig. 12 Baseline case: comparison of a) experimental PIV and b) numerical U-velocity contours.

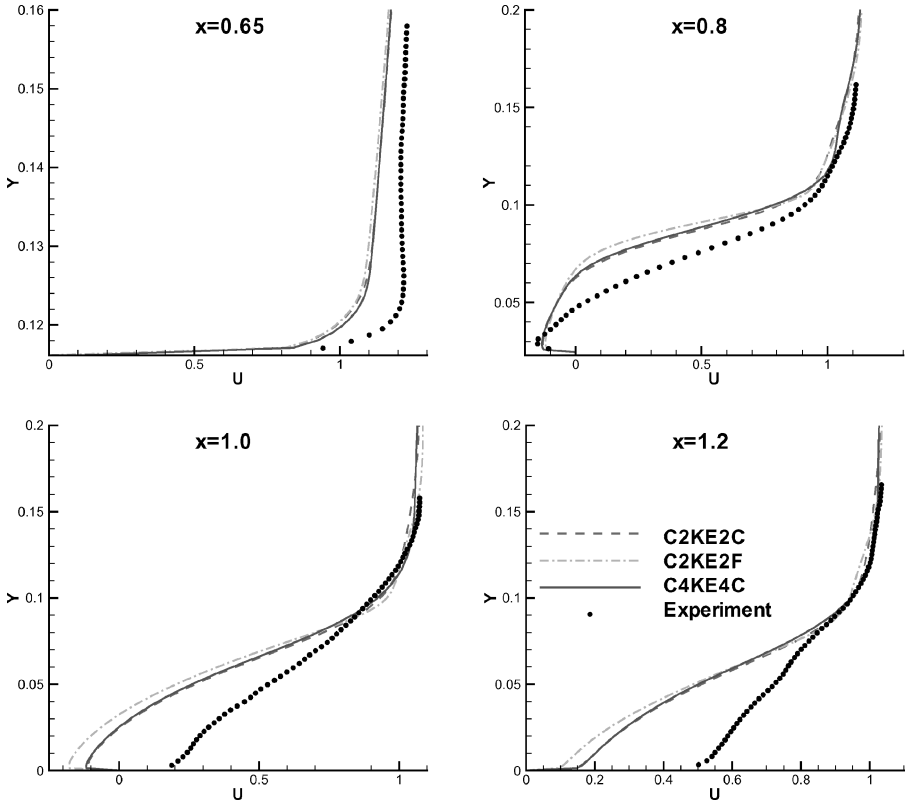

Fig. 15 Suction case: U-velocity profile comparison at $x = 0.65$, 0.8, 1.0, and 1.2.

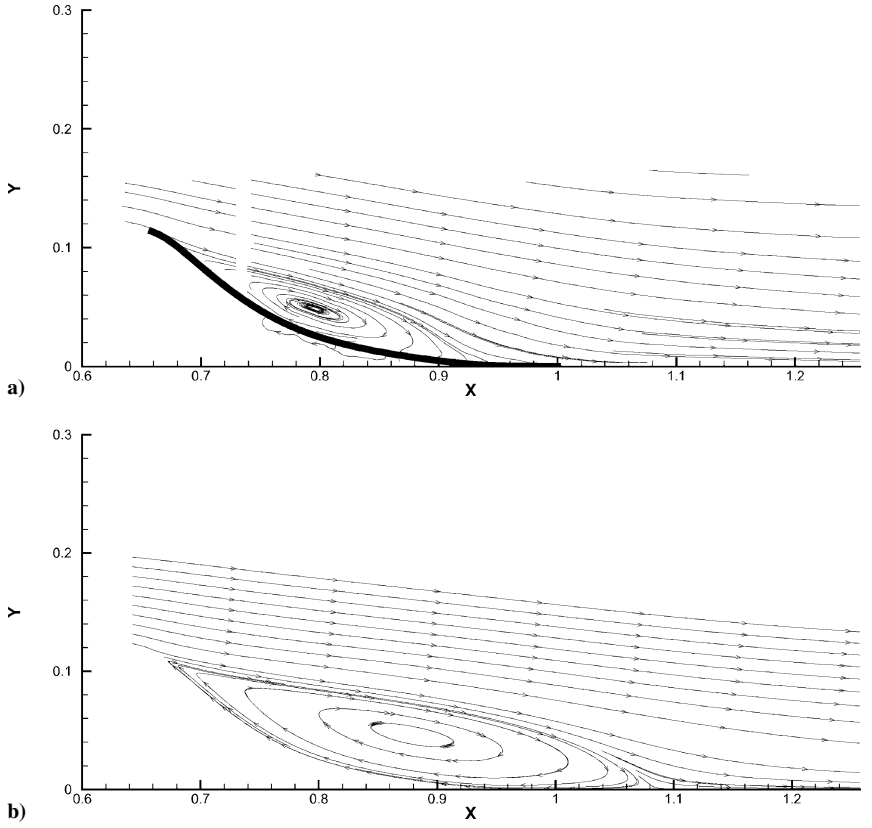

Fig. 16 Suction case: comparison of a) experimental PIV and b) numerical streamlines.

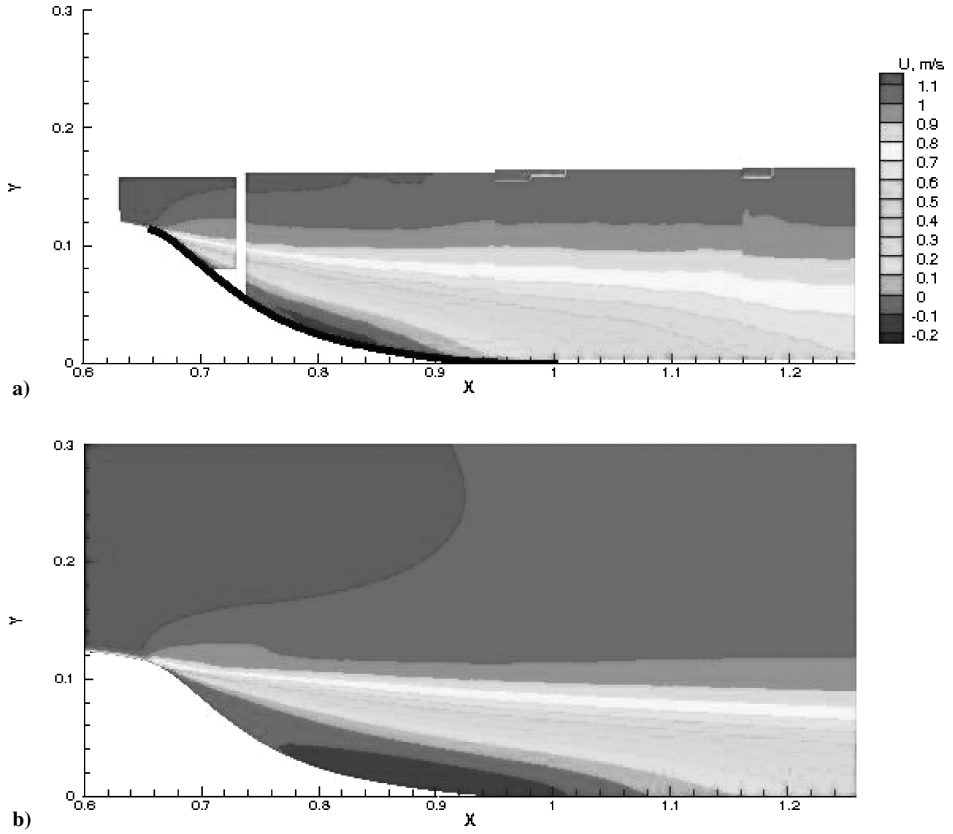

Fig. 17 Suction case: comparison of a) experimental PIV and b) numerical *U*-velocity contours.

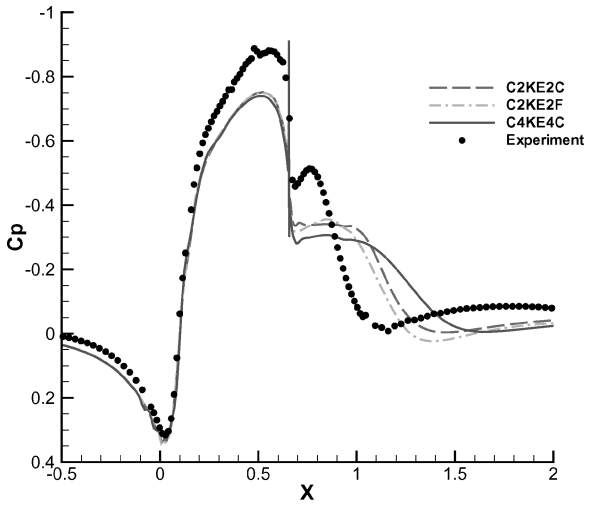

Fig. 18 Oscillating blowing and suction case: time-averaged surface pressure coefficient comparison.

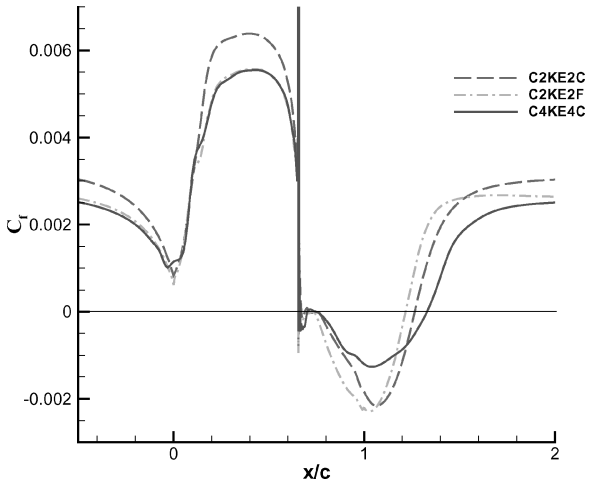

Fig. 19 Oscillating blowing and suction case: time-averaged skin-friction coefficient comparison.

scheme is the only approach that is still very close to the experimental profile. Unfortunately, at $x = 1.2$, this trend did not hold, and all of the profiles are less full than experiment, supporting the fact that reattachment for all of the simulations occurred farther downstream than seen in the experiment. This result is not unexpected because turbulence models are known for having problems accurately predicting separated flow regions.

Comparisons of the streamlines and u-velocity contours for the high-order C4KE4C case and experimental PIV data are shown in Figs. 11 and 12, respectively. Qualitative agreement between the computations and the experiment is evident. The streamline plot clearly shows that the numerical solution has a longer and thinner separation bubble than that seen experimentally. The u contours show that the region of maximum negative velocity is larger and extends more upstream in the experiment.

Two cases with flow control were also performed, one with suction only and another with oscillatory suction and blowing. Both cases were designed to use enough flow control to reduce the size of the separation bubble, but not eliminate it.

Results for the flow control case using suction are shown in Figs. 13–17. The surface pressure coefficient for the different grids and methods are compared in Fig. 13. As with the baseline case, all of the numerical solutions have a smaller magnitude in the midspan portion of the hump than that seen experimentally. Likewise, the recirculation region is not as strong and is longer than experimentally observed. The experimental flow reattachment point occurred at $x = 0.94$. The numerical solutions generated a range for the reattachment point at $1.08 \leq x \leq 1.13$ (Table 2) for the different cases. The skin-friction coefficient comparison (Fig. 14) shows a good agreement with the various schemes except for the coarse grid second-order scheme, which has the same qualitative

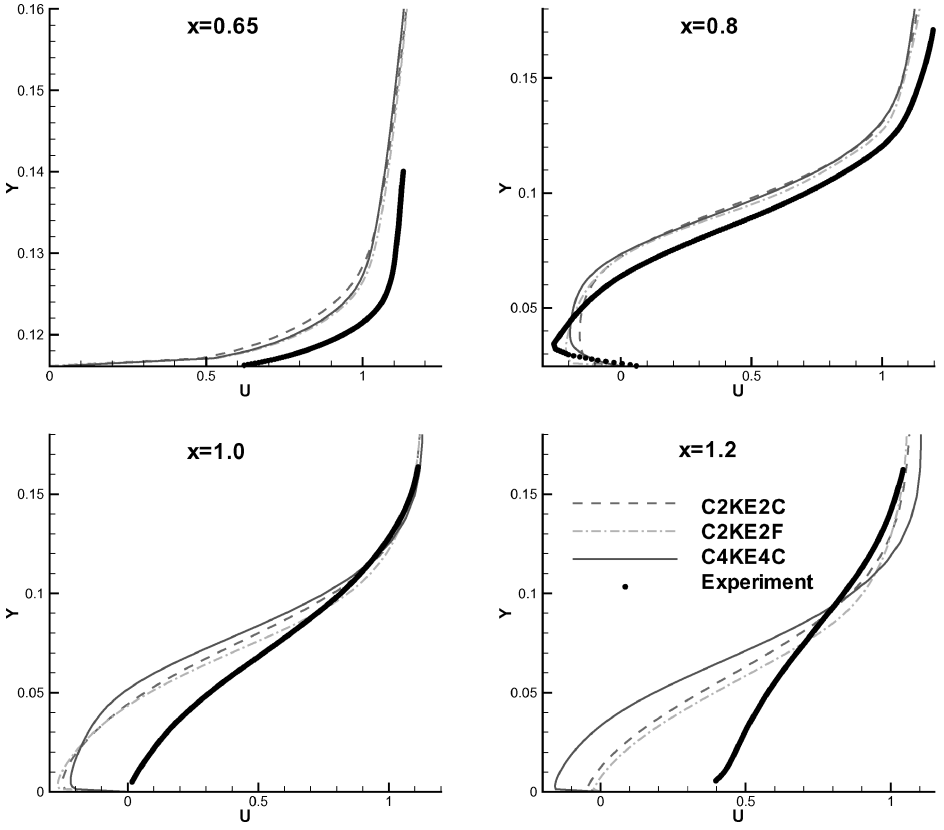

Fig. 20 Oscillating blowing and suction case: U-velocity profile comparison at $x = 0.65$, 0.8, 1.0, and 1.2.

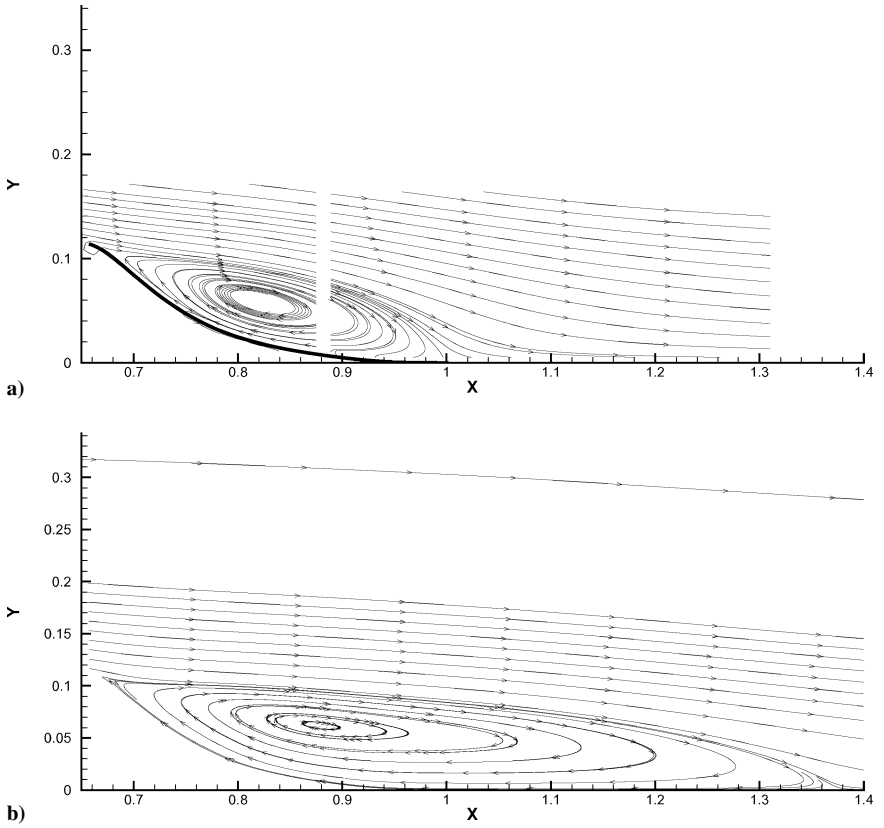

Fig. 21 Oscillating blowing and suction case: comparison of a) experimental PIV and b) numerical streamlines.

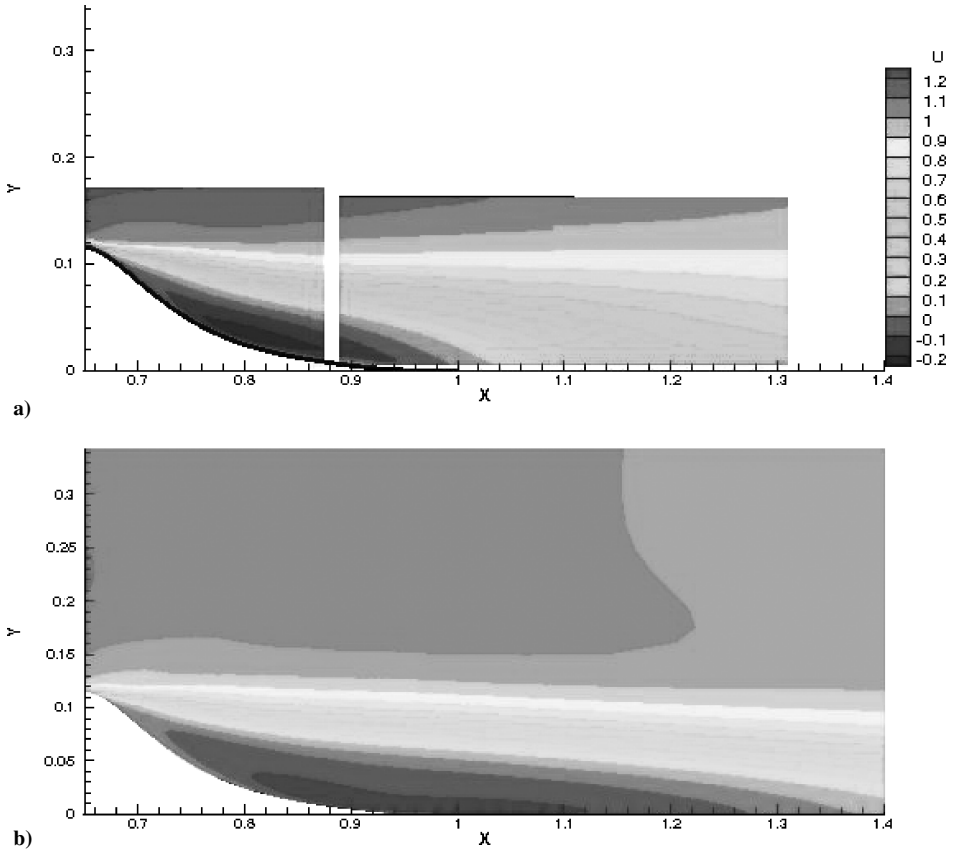

Fig. 22 Oscillating blowing and suction case: comparison of a) experimental PIV and b) numerical *U*-velocity contours.

shape, but a significantly higher magnitude over the length of the hump.

The u-velocity profiles at the same locations described for the baseline case are shown in Fig. 15. At $x = 0.65$, the velocity profile is not as full as the experimental data. At $x = 0.8$, the computed height of the separated flow is almost a factor of two larger than the experimental result. After flow reattachment for the experiment, at $x = 1.0$, the numerical simulation are still displaying a significant recirculation region. By $x = 1.2$, the numerical solutions have all reattached, but the velocity profiles have not recovered to the same extent as the experiment because reattachment occurred considerably downstream of the experimental observations.

The last comparison for the suction case is the streamlines and u-velocity contours for the experiment and the high-order numerical simulation, C4KE4C, shown in Figs. 16 and 17, respectively. The streamline Fig. 16 clearly shows the difference in size between the experiment and computed recirculation region. The experiment has a separated region that is not only shorter in length, but also much thinner and compact. The u-contours comparison (Fig. 17) shows that the reverse flow region in the numerical simulations had stronger reverse flow and was located farther downstream.

The final case with flow control used oscillating blowing and suction. A comparison of the experimental C_p with numerical solutions is given in Fig. 18. As earlier seen in the baseline and suction cases, the magnitudes of C_p from numerical solutions are smaller than the experimental findings. One interesting observation is that C_p is more sensitive in the recirculation region for the different cases than seen in the flows with no control and suction. The skin-friction coefficient comparison (Fig. 19) shows a good agreement between the fine grid second-order solution, C2KE2F, and the coarse grid compact solution, C4KE4C over the hump before separation. The coarse grid second-order solution, C2KE2C, has the same qualitative shape in this region, but has a higher magnitude. Significant variations are visible in the recirculation region between the numerical solutions. The C4KE4C solution predicts smaller velocity gradients at the wall and flow reattachment farther downstream than either of the second-order solutions.

The time-mean u-velocity profiles in Fig. 20 are shown at the same locations described for the baseline and suction cases. The velocity profile at $x = 0.65$ has the correct qualitative shape but again is not as full as the experimental profile. At $x = 0.8$, good agreement exists with the experimental result. The profiles at $x = 1.0$ and at $x = 1.2$ show that the flow is separated in all of the numerical solutions but has reattached in the experiment.

Finally, the comparison of the time-mean streamlines and u-velocity contours for the experiment and case C4KE4C for the oscillatory blowing and suction case are shown in Figs. 21 and 22, respectively. The streamline Fig. 21 shows a significantly longer separation bubble in the numerical solution than the experiment. This may indicate that URANS is not well suited for simulating highly unsteady flow control devices.

V. Conclusions

This work discussed the development of a HO-RANS approach. The high-order discretization of the k–ϵ equations was validated for flow over a flat plate and compared with a second-order accurate solution. Finally, the new approach was applied to flow over a wall-mounted hump for the flow conditions of $M_\infty = 0.10$ and $Re_c = 9.36 \times 10^5$.

Various levels of discretization accuracy were investigated for a flat plate. This portion of the study demonstrated that a second-order-accurate discretization of the k–ϵ turbulence equations dominates the solution even when high-order compact differencing is used for the flow equations. A grid-resolution study verified the expected trend that the solution reached an asymptotic state much faster with a HO-RANS methodology than with a standard second-order accurate approach.

Application of the HO-RANS technique to a wall-mounted hump was also accomplished. Simulations for the hump were completed for conditions with and without flow control and were compared to previous numerical and experimental results. Some disagreements with the experiment data were seen in the current study. Similar problems were also observed by all of the groups that studied this

configuration at the NASA workshop. Part of the discrepancies with the experimental hump surface pressure coefficient was due to wind-tunnel blockage in the experiment. Wind-tunnel blockage is believed to be responsible in part for the disagreement. Comparison of HO-RANS and second-order RANS solutions were performed. Qualitative agreement was achieved with experimental data for both high- and low-order schemes. High-order solutions on a coarse grid agreed very well with second-order solutions on a grid four times larger. The surface pressure coefficient was smaller in magnitude over the midspan of the hump and in the separated flow region than experimental results for both cases with and without flow control. The reattachment location in the numerical simulations was less than 10% farther downstream than the experimental values for the baseline case and 20% for the steady suction cases. For oscillatory blowing and suction, the numerical simulations predicted a reverse flow region that was almost twice as long as the experiment. To achieve better agreement with experimental data, future research is needed to quantify and account for effects of the wind-tunnel blockage and endplates. Better agreement might be achieved with the experiment in the separated region using more advanced techniques such as hybrid RANS/LES and LES.

Both the flat plate flow and wall-mounted hump cases demonstrated that significant net computational savings are possible when using high-order discretization for the flow and turbulence equations. For cases with separated flow, this points to the need to develop high-order methods for hybrid RANS/LES approaches.

Acknowledgments

The authors are grateful for Air Force Office of Scientific Research sponsorship under a task monitored by T. Beutner. This work was also supported in part by grants of computer time from the Department of Defense High Performance Computing Centers at the Aeronautical Systems Center and the Naval Oceanographic Office. The authors are grateful to M. White for many helpful discussions.

References

[1]Seifert, A., and Pack, L., "Active Flow Separation Control on Wall-Mounted Hump at High Reynolds Numbers," *AIAA Journal*, Vol. 40, No. 7, 2002, pp. 1363–1372.

[2]Greenblatter, D., Paschal, K., Yao, C., Harris, J., Schaeffler, N., and Washburn, A., "A Separation Control CFD Validation Test Case Part: Baseline and Steady Suction," AIAA Paper 2004-2220, June 2004.

[3]Greenblatter, D., Paschal, K., Yao, C., and Harris, J., "A Separation Control CFD Validation Test Case Part 2. Zero Efflux Oscillatory Blowing," AIAA Paper 2005-0485, Jan. 2005.

[4]Seifert, A., and Pack, L., "Compressibility and Excitation Location Effects on High Reynolds Numbers Active Separation Control," *Journal of Aircraft*, Vol. 40, No. 1, 2003, pp. 110–119.

[5]Pack, L., and Seifert, A., "Dynamics of Active Separation Control at High Reynolds Numbers," AIAA Paper 2000-0409, Jan. 2000.

[6]Postl, D., Wernz, S., and Fasel, H., "Case 3: Direct Numerical Simulation on the Cray X1," *CFD Validation of Synthetic Jets and Turbulent Separation Control Workshop*, Vol. 1, NASA Langley Research Center, March 2004, pp. 3.3.1–3.3.5.

[7]Ekaterinaris, J., "On the Use of High-Order Methods for Complex Aerodynamic Problems," AIAA Paper 2004-0431, Jan. 2004.

[8]De Rango, S., and Zingg, D., "Aerodynamic Computations Using a Higher-Order Algorithm," AIAA Paper 99-0167, Jan. 1999.

[9]De Rango, S., and Zingg, D., "Further Investigation of a Higher-Order Algorithm for Aerodynamic Computations," AIAA Paper 2000-0823, Jan. 2000.

[10]De Rango, S., and Zingg, D., "High-Order Aerodynamic Computations on Multi-Block Grids," AIAA Paper 2001-2631, June 2001.

[11]De Rango, S., and Zingg, D., "Higher-Order Spatial Discretization for Turbulent Aerodynamic Computations," *AIAA Journal*, Vol. 39, No. 7, 2001, pp. 1296–1304.

[12]Balakumar, P., "Computations of Flow over a Hump Model Using Higher Order Method with Turbulence Modeling," AIAA Paper 2005-1270, Jan. 2005.

[13]Rizzetta, D., and Visbal, M., "Large-Eddy Simulation of Supersonic Cavity Flowfields Including Flow Control," *AIAA Journal*, Vol. 41, No. 8, 2003, pp. 1452–1462.

[14]Rizzetta, D., and Visbal, M., "Application of Large-Eddy Simulation to Supersonic Compression Ramps," *AIAA Journal*, Vol. 40, No. 8, 2002, pp. 1574–1581.

[15]Morgan, P., Visbal, M., and Rizzetta, D., "A Parallel High-Order Flow Solver for Large-Eddy and Direct Numerical Simulation," AIAA Paper 2002-3123, June 2002; also *Journal of Scientific Computing* (to be published).

[16]Morgan, P., and Visbal, M., "Large-Eddy Simulation of Airfoil Flows," AIAA Paper 2003-0777, Jan. 2003.

[17]Morgan, P., and Visbal, M., "Large-Eddy Simulation Modeling Issues for Flow Around Wing Sections," AIAA Paper 2003-4152, June 2003.

[18]Launder, B., and Sharma, B., "Application of the Energy Dissipation Model of Turbulence to the Calculation of Flow Near a Spinning Disc," *Letters in Heat and Mass Transfer*, Vol. 1, No. 2, 1974, pp. 131–138.

[19]Gordnier, R., "Computational Study of a Turbulent Delta-Wing Flowfield Using Two-Equation Turbulence Models," AIAA Paper 96-2076, June 1996.

[20]Beam, R., and Warming, R., "An Implicit Factored Scheme for the Compressible Navier–Stokes Equations," *AIAA Journal*, Vol. 16, No. 4, 1978, pp. 393–402.

[21]Gordnier, R., and Visbal, M., "Numerical Simulation of Delta-Wing Roll," AIAA Paper 93-0554, Jan. 1993.

[22]Pulliam, T., and Chaussee, D., "A Diagonal Form of an Implicit Approximate-Factorization Algorithm," *Journal of Computational Physics*, Vol. 39, No. 2, 1981, pp. 347–363.

[23]Melville, R., and Morton, S., "Fully Implicit Aeroeelasticity on Overset Grid System," AIAA Paper 98-0521, Jan. 1998.

[24]Morton, S., Melville, R., and Visbal, M., "Accuracy and Coupling Issues of Aeroelastic Navier–Stokes Solutions on Deforming Meshes," *Journal of Aircraft*, Vol. 35, No. 5, 1998, pp. 798–805.

[25]Lutton, M., and Visbal, M., "Time-Accurate Validation of the Chimera Method for Unsteady Vortical Flows," AIAA Paper 96-2077, June 1996, p. 14.

[26]Lele, S., "Compact Finite Difference Schemes with Spectral-Like Resolution," *Journal of Computational Physics*, Vol. 103, 1992, pp. 16–42.

[27]Gaitonde, D., and Visbal, M., "High-Order Schemes for Navier–Stokes Equations: Algorithm and Implementation into FDL3DI," U.S. Air Force Research Labs., AFRL-VA-WP-TR-1998-3060, Wright–Patterson AFB, OH, Aug. 1998.

[28]Visbal, M., and Gaitonde, D., "High-Order Accurate Methods for Complex Unsteady Subsonic Flows," *AIAA Journal*, Vol. 37, No. 10, 1999, pp. 1231–1239.

[29]Visbal, M., and Rizzetta, D., "Large-Eddy Simulation on Curvilinear Grids Using Compact Differencing and Filtering Schemes," *Journal of Fluids Engineering*, Vol. 124, No. 4, 2002, pp. 836–847.

[30]Visbal, M., and Gaitonde, D., "Very High-Order Spatially Implicit Schemes for Computational Acoustics on Curvilinear Meshes," *Journal of Computational Acoustics*, Vol. 9, No. 4, 2001, pp. 1259–1286.

[31]Pointwise, I., *Gridgen User Manual Version 15*, Pointwise, Inc., Fort Worth, TX, 2003.

[32]Visbal, M., and Gaitonde, D., "On the Use of High-Order Finite-Difference Schemes on Curvilinear and Deforming Meshes," *Journal of Computational Physics*, Vol. 181, Sept. 2002, pp. 155–185.

C. Rumsey
Guest Editor